

An Investigation of Equivalence Principle Violations Using Solar Neutrino Oscillations in a Constant Gravitational Potential

J. R. Mureika*

*Department of Computer Science
University of Southern California
Los Angeles, California 90068 USA*

October 27, 2019

Abstract

Neutrino oscillations induced by a flavor-dependent violation of the Einstein Equivalence Principle (VEP) have been recently considered as a suitable explanation of the solar ν_e deficiency. Unlike the MSW oscillation mechanism, the VEP mechanism is dependent on a coupling to the local background gravitational potential Φ . We investigate the differences which arise by considering three-flavor VEP neutrinos oscillating against fixed background potentials, and against the radially-dependent solar potential. This can help determine the sensitivity of the gravitationally-induced oscillations to both constancy and size (order of magnitude) of Φ . In particular, we consider the potential of the local supercluster, $|\phi_{SC}| = 3 \times 10^{-5}$, in light of recent work suggesting that the varying solar potential has no effect on the oscillations. The possibility for arbitrarily large background potentials in different cosmologies is discussed, and the effects of one such potential ($\Phi = 10^{-3}$) are considered.

1 Introduction

A resurgence of flavor-oscillation solutions to the Solar Neutrino Problem has recently inundated the world of particle astrophysics. Of these, the two main competitors are the tried and true MSW mechanism [1, 2], and

*newt@java.usc.edu

the more radical VEP (for “Violation of the Equivalence Principle”) oscillation model [3]. The MSW mechanism is often the more seriously considered one, due to the basic underlying hypothesis of VEP, which requires a generation–dependent violation of the Einstein Equivalence Principle (*i.e.* flavor–dependent coupling to the background gravitational potential Φ) in the neutrino sector, and tends to give most physicists a headache. Conversely, there is no experimental justification for any flavor of neutrino to have mass, so MSW can also be considered a large assumption.

Another consideration is the number of flavors with which to work. Many studies of neutrino oscillations [4, 5] take the simpler two–neutrino approach by only considering the effects of a flavor eigenstate $|\nu_W\rangle = (\nu_e, \nu_\mu)^T$. There are at least three flavors known in nature, though, and various studies [6, 7] have suggested that the two–flavor model short–changes the viable solution set by considering only a minute portion of the overall parameter space. The authors of [8] suggest that three–flavors are sufficient to solve the SNP.

Proper experimental results from solar neutrino detectors could help isolate the individual values of the mass eigenvalues and mixing angles which contribute to oscillations. Experimental detection of oscillations induced by the MSW mechanism can yield determination of the neutrino energy eigenvalue differences $\Delta m_{ij}^2/(2E)$, and hence the neutrino masses m_i . If VEP is the true underlying mechanism, the analogue of the energy eigenvalue difference is $2E\Phi\Delta f_{ij}$. As long as we are aware of the background potential Φ that causes the oscillations, we can isolate the values Δf_{ij} , and thus the individual f_i s. While experimental verification of MSW can teach us new neutrino physics, a detection of VEP oscillations can additionally yield new information on solar astrophysics and General Relativity (the universality of the equivalence principle).

For solar neutrinos, one would generally expect $\Phi = \phi_\odot(r)$, *i.e.* that of the solar interior. However, there is some debate as to whether or not the propagating neutrinos feel the effects of a potential *difference*, or whether they feel the overall effects of the strongest potential [9]. If the latter is the case, then the gravitational potential of the local supercluster $|\phi_{SC}| = 3 \times 10^{-5}$ overwhelms the former by almost a factor of 10. In effect, the solar neutrino problem has actually become the *solar* neutrino problem: without proper knowledge of the background potential which contributes to the flavor oscillations, we can only learn as much new physics as we could in the MSW case. That is to say, we can only determine that neutrinos *do* oscillate, but not their gravitational eigenvalues.

This then raises the question of how much of a difference the choice of

potential makes in the overall process. The following paper will examine the dependence on potential energy of flavor oscillations in a three-generation framework, from two specific standpoints. To begin with, we will compare the effects of the radially-dependent solar potential $\phi_{\odot}(r)$ with a constant one of equal magnitude (the solar surface potential, $|\phi_{\odot}(R_{\odot})| = 2.12 \times 10^{-6}$ [10]). This will give an indication of the sensitivity of the data to variations over a fixed magnitude. Secondly, a comparison will be made of several constant potentials, to examine dependence on varying magnitudes. These will primarily include the solar surface potential, and the local supercluster $|\phi_{SC}| = 3 \times 10^{-5}$. An arbitrarily large potential of the order $\Phi = 10^{-3}$ will be considered, as well, for reasons discussed in section 4.

2 MSW and VEP Oscillation Mechanisms

At heart, the MSW and VEP mechanisms are the same. Both rely on the existence of two distinct eigenstates of the neutrinos. In the former case, there are mass and electroweak eigenstates, $|\nu\rangle_M$ and $|\nu\rangle_W$. For the latter, the mass eigenstate is replaced with a gravitational one, $|\nu\rangle_G$, as the VEP neutrinos are considered massless¹. The equations of motion are diagonal in the mass/gravitational (M,G) basis,

$$i \frac{d}{dr} |\nu\rangle_{M,G} = H |\nu\rangle_{M,G} , \quad (1)$$

where (1) is derivable from the Pauli equation [7]. To investigate neutrino flavor dynamics, the (M/G) states $|\nu\rangle_{M,G}$ are rotated to the electroweak basis via $|\nu\rangle_W = V |\nu\rangle_{M,G}$, $V \in SU(N)$ for N flavors². Due to charged current interactions in the ν_e sector, an additional interaction $\mathcal{A} = \text{diag}(\sqrt{2}G_F N_e, 0, 0, \dots)$ must be added, giving the final equation of motion as

$$i \frac{d}{dr} |\nu\rangle_W = \{V H V^{-1} + \mathcal{A}\} |\nu\rangle_W = H' |\nu\rangle_W . \quad (2)$$

for neutrinos of energy E . Here, $\mathcal{A}(r) = \text{diag}(2\sqrt{2}G_F N_e(r), 0, 0, \dots)$, with Fermi's constant G_F , and the radially-dependent solar electron density $N_e(r)$. Subtracting an overall factor of H'_{11} (and hence an unobservable

¹There has been some investigation of the possibility of massive VEP neutrinos, but those are not considered here. See [11] for further information.

²Although V is a four parameter matrix (3 real rotations and a complex phase), we do not consider CP violations here, and thus eliminate the complex phase.

phase in the wavefunction) from (2), and re-diagonalizing, one obtains eigenstates dependent of either values of $\Delta m_{ij}^2/2E$ or $2E|\Phi|\Delta f_{ij}$, $i, j \neq 1, i \neq j$. The main signature of VEP is its inverse dependence on the neutrino energy E , as compared to MSW.

3 Three-Flavor VEP Formalism

A brief review of the underlying formulation of the VEP mechanism is required before proceeding. Three-flavor oscillations take place due to the existence of two non-trivial spinor eigenbases, $|\nu\rangle_G = (\nu_1, \nu_2, \nu_3)^T$, $|\nu\rangle_W = (\nu_e, \nu_\mu, \nu_\tau)^T$, related by a rotation matrix $V_3 \in SO(3)$ (*i.e.* no CP violations),

$$|\nu\rangle_W = V_3|\nu\rangle_G . \quad (3)$$

The gravitational eigenbasis evolves according to the massless Dirac equation

$$i\mathcal{D}\psi_G = 0 , \quad \psi_G \equiv \sum_k (|\nu\rangle_G)_k \exp\{-iE_k t\} , \quad (4)$$

The Hamiltonian derived from Eq.(4) becomes off-diagonal under the change of basis (3),

$$H' = V_3 H(\Phi) V_3^{-1} + \mathcal{A}(r) , \quad (5)$$

with

$$\begin{aligned} H(\Phi) &= 2E|\Phi| \begin{pmatrix} f_1 & 0 & 0 \\ 0 & f_2 & 0 \\ 0 & 0 & f_3 \end{pmatrix} , \\ \mathcal{A}(r) &= 2\sqrt{2}G_F N_e(r) \text{diag}\{1, 0, 0\} . \end{aligned} \quad (6)$$

We explicitly express the dependence on the potential of $H = H(\Phi)$ for our later consideration of the various forms of $\Phi = \{\phi_\odot(r), \phi_{SC}, \phi_{SD}\}$, but omit it for the other Hamiltonians (and assume its dependence to be understood in these cases). The matrix $\mathcal{A}(r)$ is introduced by the charged-current interactions of the ν_e s (hence the triviality $\mathcal{A}_{ij} = 0 \forall \{i, j\} \neq \{1, 1\}$), and results in a shift in the energy eigenvalues E_k from their values in 4. A new basis $|\nu\rangle_{MG}$ and set of corrected eigenvalues $\{E_1'', E_2'', E_3''\}$ may be found by re-diagonalization

$$H'' = V_3^m H' (V_3^m)^{-1} , \quad (7)$$

where $V_3^m = V_3^m(\theta_{12}^m, \theta_{13}^m, \theta_{23}^m)$ is the corrected rotation matrix, with matter-enhanced angles (see [7] for the definition of these, or [12, 13] for their MSW equivalent).

The wave equation may now be solved, subject to the modified Hamiltonian H'' , and the subsequent survival probabilities for neutrino eigenstates can be found. For solar neutrinos, the value of interest is $\langle P(\nu_e \rightarrow \nu_e) \rangle$, since most detectors to date are sensitive only to first-generation neutrinos (this is not true of future detectors such as Superkamiokande or SNO, which can detect neutral current interactions from all flavors). Averaged over the Earth-Sun distance, the expression obtained is

$$\begin{aligned} \langle P(\nu_e \rightarrow \nu_e) \rangle &= \sum_{i,j=1}^3 |(V_3)_{1i}|^2 |(P_{LZ})_{ij}|^2 |(V_3^m)_{1j}|^2 \\ &= c_{m12}^2 c_{m13}^2 \left\{ (1 - P_1) c_{12}^2 c_{13}^2 + P_1 s_{12}^2 c_{13}^2 \right\} \\ &\quad + s_{m12}^2 c_{m13}^2 \left\{ P_1 (1 - P_2) c_{12}^2 c_{13}^2 + (1 - P_1)(1 - P_2) s_{12}^2 c_{13}^2 + P_2 s_{13}^2 \right\} \\ &\quad + s_{m13}^2 \left\{ P_1 P_2 c_{12}^2 c_{13}^2 + P_2 (1 - P_1) s_{12}^2 s_{13}^2 + (1 - P_2) s_{13}^2 \right\} . \end{aligned} \quad (8)$$

which is a function of the matter-enhanced mixing angles $\theta_{13}^m, \theta_{13}^m$ and eigenvalues differences $\Delta F_{21}, \Delta F_{31}$, and the regular (vacuum) equivalents θ_{12}, θ_{13} , and $\Delta f_{21}, \Delta f_{31}$. Note that $\langle P(\nu_e \rightarrow \nu_e) \rangle$ does not depend on interactions between the second and third flavors, $\nu_\mu \rightarrow \nu_\tau, \nu_\tau \rightarrow \nu_\mu$.

The results of [7, 14] offer insights into the fundamental theoretical and observational differences between the VEP and MSW mechanisms. The overall conclusion was found to be that the addition of the third neutrino flavor can significantly enhance the overall allowed parameter space from that of the two-flavor model. Unique experimental signatures in observed ν_e fluxes can also arise between the VEP and MSW, which could be used to differentiate between mechanisms.

4 A Potential Problem!

While most papers on VEP tend to agree on the form of the oscillation mechanism³, there is some debate as to which background potential is at work. Most works have assumed that neutrinos feel the potential difference of the sun from their creation points, to their exit on the surface, which ranges between $\sim (-7, -2) \times 10^{-6}$ [7]. Alternatively, [9] suggests that the neutrinos feel instead the constant background potential of the Local Supercluster (Great Attractor), which in the neighborhood of the solar system is $|\phi_{SC}| = 3 \times 10^{-5}$. This overpowers the surface potential of the Sun by almost a factor of 10. Results from the COBE data suggest that the dominant local background potential is very close to this value [15].

Furthermore, while the current dominant potential in the local neighborhood seems to be that of ϕ_{SC} , one should be careful to consider the overall potential contribution of the Universe. Following [16], the local background potential can be expressed as the sum of all contributing potentials, $\Phi_{local} = \phi_{\oplus} + \phi_{odot} + \phi_{MW} + \phi_{SC} + \phi_U + C$. The contributors of the potentials are, respectively, the Earth, Sun, Milky Way, Local Supercluster, the Universe, and an arbitrary constant C . This is different from Equation (3) of [16] in that the (dominant) potential ϕ_{SC} has been added. The constant C comes from an arbitrary cosmological model that might be at work, but is undetectable by our standards. That is, as expressed in [16], “we cannot ‘step outside the universe’ to [measure the actual value of C]”⁴. Hence, a future cosmology might contain a C such that $\Phi_{local} \sim C$. If C is sufficiently large, it will overwhelm the other contributors. For this work, we will assume the value of $C = 10^{-3}$, and denote this by ϕ_{SD} .

From solar neutrinos alone, we can only hope to isolate the values of $\Delta f_{ij}\Phi$ (see, for example, [17], and not the individual eigenvalues Δf_{ij} . According to the aforementioned product, the values of Φ and of Δf_{ij} are inversely linked. So, by considering the effects of the Local Supercluster ϕ_{SC} over the effects of the solar potential $\phi_{\odot}(r)$, one is effectively shifting the values of the violation parameters down by an order of magnitude. At first glance, this would seem to not be a big problem, but it should be noted that shifts of this magnitude can strongly affect the oscillation behavior for

³There is a brief mention in [4] of an alternative form of equivalence principle violation, based on neutrinos coupling to $\nabla\Phi$, instead of Φ , in some string theories.

⁴This can be thought of as a type of philosophical argument, along the lines of “how do we know the reality is not just an illusion?”, but with actual physical evidence to support it!

critical values of mixing angle and EEP-violations from the other flavor.

5 $\langle P(\nu_e \rightarrow \nu_e) \rangle$ Curves and Surfaces

For two-flavor analyses of neutrino oscillations, it is useful to study the averaged ν_e survival probability curves $\langle P(\nu_e \rightarrow \nu_e) \rangle$. Such plots are generally expressed as functions of the argument $E\Delta f$, scaled to an appropriate value. These curves indicate the overall behavior of $\langle P(\nu_e \rightarrow \nu_e) \rangle$ with respect to values of violation parameters Δf (*i.e.* f_1 and f_2) and mixing angle θ . In particular, it is of use to examine the small and large-mixing angle limits.

For two flavors, the resonant boundary for solar neutrinos is determined by equating the resonance density

$$(N_e)_{res} = \frac{\sqrt{2}|\phi_{\odot}(r)|E\Delta f \cos 2\theta_G}{G_F}, \quad (9)$$

Since the density of the sun is strictly decreasing from its center, then if the resonance density for a neutrino is greater than the density at which it was created, it will never undergo matter-enhanced oscillations and will propagate as in vacuum (note that they may still undergo vacuum oscillations). Using the radial solar potential $\phi_{\odot}(r)$, one obtains a resonance boundary of $\Delta f \sim 2 \times 10^{-12}$ for neutrinos of energies $E_{\nu} > 0.2$ MeV [4].

An extension to a three flavor model requires something extra, though. Instead of just one specific curve for θ_{12} (the equivalent of the two-flavor angle θ), there can be a whole family of curves $\{\langle P(\nu_e \rightarrow \nu_e) \rangle\}$ corresponding to the same θ_{12} . These are, of course, determined by different values of θ_{13} , and imply that the large and small limits of θ_{13} must also be considered. Hence, it becomes apparent that an examination of a *probability surface* is in order.

These surfaces are of use in three-flavor oscillation dynamics as they demonstrate the full range of behavior of $\langle P(\nu_e \rightarrow \nu_e) \rangle$ for all values of $\Delta f_{i1}\Phi$ for a given set of θ_{12}, θ_{13} . This includes regions for which neutrinos with resonance densities above the maximal solar electron density $(N_e)_{max}^i = 100g\text{ cm}^{-3}$. Again, if the resonance density for a neutrino i exceeds this value, the neutrino will not feel matter-enhancement, and will propagate as in vacuum. The resonance density for each flavor is determined by the generalization of (9) to three flavors, by replacing Δf with Δf_{ij} for the $\nu_i \rightarrow \nu_j$ resonances.

Note that the region encompassed by these surfaces includes areas where $\Delta f_{21} > \Delta f_{31}$. This corresponds to a broken hierarchy in the eigenstates

(*i.e.* $f_2 > f_3$). We would like to think that nature would follow a hierarchical ladder between generations, but there is nothing which physically rules out the possibility of breaking this. Indeed, the behavior of $\langle P(\nu_e \rightarrow \nu_e) \rangle$ does exhibit noticeable changes when the hierarchy is broken. In particular, this generates a change in the values of the matter-enhanced mixing angles θ_{21}^m and θ_{31}^m . This change is less apparent for small vacuum mixing angles, while it can create sizable differences for large vacuum angles [7].

It should be noted that these plots show the survival probabilities for 8B ν_e s⁵, the easiest of the solar neutrino spectrum to detect. The majority of the events recorded in the Homestake (${}^{37}Cl$), as well as all events detected by Kamiokande, are of this type, due to their extremely high ranging energy spectrum of [0, 15] MeV. The figures herein have been calculated using the most recent solar neutrino data and Standard Solar Model data available [19, 20].

The expression for $(N_e)^{res}$ in (9) is clearly a function of the background potential $\phi_{\odot}(r)$. Rearranging this, it is obvious that

$$\Delta f = \frac{(N_e)_{max} G_F}{\sqrt{2} E |\phi_{\odot}(r)|}, \quad (10)$$

i.e. the resonance boundary varies inversely with the potential. So, there should be a decreasing limits on the values of Δf which permit resonance as the potential increases. For the cases we concern ourselves with here, these boundaries should approximately (within an order of magnitude) occur at $\Delta f \sim 10^{-11}$ for ϕ_{SC} and $\Delta f \sim 10^{-13}$ for ϕ_{SD} .

In addition to the 8B ν_e s, the other main type of detectable neutrino is the low energy pp-neutrino, resulting from the proton-proton chain reaction. These are emitted over an energy spectrum ranging to 0.42MeV. Since their maximal energy is at least one order of magnitude different from the maximal 8B neutrino energy, then the overall product $E\Delta f_{ij}$ can shift by the same order of magnitude. It was observed in [7] that this shift can result in different resonant behavior between the reaction types of solar neutrinos, such that some can exist under the resonant barrier ($2E\Delta f_{ij}/10^{-18}\text{MeV} \approx 10^6$), while others can be over. The crux of this is that certain neutrino types will be subject to resonant behavior (for $2E\Delta f_{i1} < 10^6$, in units of 10^{18}MeV^{-1}), while certain types will propagate as in vacuum ($2E\Delta f_{i1} > 10^6$). While this analysis is restricted to 8B neutrinos, the interested reader

⁵These originate from the thermonuclear decay reaction ${}^8B \rightarrow {}^7Be + \nu_e$; for more information on solar neutrino-producing reactions, see [18].

should reference [7] for an appropriate discussion.

6 Discussion of Figures

As previously mentioned, this work considers two distinct cases of survival probabilities, as a function of background potential energy. We first consider the dependence on $\langle P(\nu_e \rightarrow \nu_e) \rangle$ curves as a function of variability in potential over a specific order of magnitude, and secondly as a function of variability of order of magnitude.

6.1 $\phi_{\odot}(r)$ v.s. $\phi_{\odot}(R_{\odot})$

It was noted in [7] that there is a strong influence from the θ_{13} contribution of the third flavor. In particular, for large θ_{13} , the survival probabilities for ν_e become effectively $\langle P(\nu_e \rightarrow \nu_e) \rangle \sim \sin^2 \theta_{13}$. This is clearly evident from Figures 1,2, which demonstrate the behavior of $\langle P(\nu_e \rightarrow \nu_e) \rangle$ from solar neutrino data in the small and large θ_{12} range, for small θ_{13} . The end result of the difference in potential presents itself as a horizontal shift to the right for $\langle P(\nu_e \rightarrow \nu_e) \rangle(\phi_{\odot}(R_{\odot}))$ when the slices are considered. The shape of the curve is preserved, which suggests that the change in potential has merely shifted the resonance density by an overall constant. Both curves assume the same values before and after this barrier. The portions of the curve for which $2E\Delta f_{21} > 5 \times 10^6$ correspond to broken hierarchy between the violation parameters $\Delta f_{i1}, i = 2, 3$.

Meanwhile, the story for small θ_{13} is set to a somewhat different tune. We observe vastly different behavior for both curves in each case of small and large θ_{12} (Figures 3,4). Both plots show that the the survival probability $\langle P(\nu_e \rightarrow \nu_e) \rangle(\phi_{\odot}(R_{\odot}))$ is greater than $\langle P(\nu_e \rightarrow \nu_e) \rangle(\phi_{\odot}(r))$. The shift in the location of the resonance boundary

6.2 Order of Magnitude Dependence

In contrast to the previous section, there is a noticeable difference in $\langle P(\nu_e \rightarrow \nu_e) \rangle$ curves and surfaces when the order of magnitude of the effective potential Phi is considered. This shift has large implications in particular when it comes to deciding which potential is at work, if the VEP mechanism is correct. Indeed, the evidence presented here could help point to the correct choice, subject to experimental verification (*e.g.* 8B flux spectra can be directly computed with knowledge of P_{surv}).

For the purposes of this discussion, both the survival probability curves and surfaces will be examined for select choices of the potential. As in Section 6.1, the small and large θ_{12} (fixed θ_{13} large) curves are presented in Figures 5,6. The chosen potentials here are $\phi_{\odot}(r)$, ϕ_{SC} , and ϕ_{SD} . It is assumed that $\phi_{\odot}(R_{\odot})$ will vary as discussed in the previous section, and thus is not considered here.

Figure 5 represents the small-angle mixings for both 12- and 13-resonances. These curves correspond to a choice of $\Delta f_{31} = 10^{-13}$, at a fixed value of $2E\Delta f_{31} = 2 \times 10^6$. In this case, each potential induces a drastically different shape for each curve. The choice of $2E\Delta f_{31}$ places the Solar curve in the double-resonance region (the ν_e can resonate to both ν_{μ} and ν_{τ}), while the ϕ_{SD} curve allows only $\nu_e \rightarrow \nu_{\mu}$ resonances. In fact, the shape of this curve approaches that for two-flavor non-adiabatic resonance [7]. By referencing Figure 7, it is evident that the plots for each Φ represent equivalent slices for $\phi_{\odot}(r)$ at different values of $2E\Delta f_{31}$ (in this case, roughly in the range 5 – 7).

A similar analysis hold true for the other cases of small and large θ_{12}, θ_{13} , and thus will not be discussed further. To support the claim that the $\langle P(\nu_e \rightarrow \nu_e) \rangle$ surfaces for each value of Φ are shifting in parameter space, Figure 8 is offered for comparison with Figure 7. This is the resulting surface for $\Phi = \phi_{SC}$. In addition, Figures 9,10 present the case for $s_{12}^2 = 0.8, s_{13}^2 = 0.001$. It is clear from both comparisons that the overall shapes of the surfaces are the same, up to a shift of an overall constant. As suggested, this corresponds to an order of magnitude shift in the resonance boundary.

Figures 11 and 12 are overhead projections of Figures 9,10 in the $(2E\Delta f_{21}, 2E\Delta f_{31})$ plane. The lighter-shade triangular-shaped wedge at the center depicts two of the features discussed here. The vertical boundary represents the resonance boundary, where $(N_e)^{cr} > (N_e)_{max}$ for each neutrino, while the diagonal one shows the intersection of the plane $\Delta f_{21} = \Delta f_{31}$. It can be seen that the former shifts as discussed according to the potential Φ , while obviously the latter remains fixed.

7 What's All This, Then?

It thus becomes apparent that the same type of shifting effect as that noted in [7] could conceivably occur, depending on the choice of gravitational potentials affecting the VEP oscillations. Whereas before it was thought that VEP oscillations were singly dependent on the product $\Phi\Delta f_{ij}$, these results

suggest that perhaps the value of the background potential Φ can indeed be constrained by the resultant neutrino data. The figures presented here immediately determine the observed energy spectrum of ${}^8\text{B}$ neutrinos, and many future neutrino observatories could detect these variations. As with the results in [7, 14], it is found that the shapes of the probabilities are strongly determined by the size of θ_{13} , and small 13-angle oscillations provide a much more diverse spectrum of $\langle P(\nu_e \rightarrow \nu_e) \rangle$ curves for different input values (in this case, the potential Φ).

Alternatively, what could also solve such a problem, should VEP be the mechanism at work, is the detection and subsequent spectrum analysis of extra-solar neutrinos from sources whose gravitational potential is known to either great accuracy or reliability. Various papers have addressed the detection of such high-energy intergalactic neutrinos subject to the VEP mechanism [21].

Additionally, the discovery of a possible “gravitationally-induced quantum phase” was recently discussed in the literature [22]. While the reference treatment deals with MSW neutrinos which can possibly experience a phase shift due to interactions with strong gravitational sources, it may be possible to extend the analogy to VEP neutrinos [23]. Should such an extension be possible, then it may be possible to determine the potential felt in the vicinity of the Sun, since the gravitationally-induced quantum mechanical phases of [22] would be functions of the source potential (hence the product $\Delta f_{ij}\Phi_{Source}$, and not just the product $\Delta f_{ij}\Phi_{SolarSystem}$). These conclusions are as of yet unverified.

Acknowledgements

I thank R. B. Mann profusely for proof-reading the manuscript, for offering great insight and suggestions, and for allowing me to perform calculations on his computer.

References

- [1] S. P. Mikheyev and A. Yu. Smirnov, *Yad. Fiz.* **42**, 1441 (1985); S. P. Mikheyev and A. Yu. Smirnov, *Phys. Lett.* **B21**, 560 (1988).
- [2] L. Wolfenstein, *Phys. Rev.* **D17**, 2369 (1978).
- [3] M. Gasperini, *Phys. Rev.* **D38**, 2635 (1988).

- [4] J. N. Bahcall, P. I. Krastev, and C. N. Leung, Phys. Rev. **D52**, 1770 (1995).
- [5] N. Butler *et al.*, Phys. Rev. **D47**, 2615 (1993).
- [6] G. L. Fogli, E. Lisi, and D. Montanino, Astropart. Phys. **4**, 177 (1995).
- [7] J. R. Mureika and R. B. Mann, Phys. Rev. **D54**, 2761 (1996).
- [8] A. Acker and S. Pakvasa, hep-ph/9611423.
- [9] A. Halprin, C. N. Leung, and J. Pantaleone, Phys. Rev. **D53**, 5365 (1996)
- [10] S. Weinberg, *Gravitation and Cosmology: Principles and Applications of the General Theory of Relativity*, John Wiley and Sons, Inc. (1972).
- [11] H. Minakata and H. Nunokawa, KEK-TH-396/TMUP-HEL-9402, (hep-ph 9405239) (April 1994).
- [12] H. W. Zaglauer and K. H. Schwarzer, Phys. Lett. **B198** 556 (1987).
- [13] V. Barger *et al.*, Phys. Rev. **D22**, 2718 (1980).
- [14] J. R. Mureika and R. B. Mann, Phys. Lett. **B368**, 112 (1996)
- [15] http://www.gsfc.nasa.gov/astro/cobe/cobe_home.html, COBE home page. The COBE datasets were developed by the NASA Goddard Space Flight Center under the guidance of the COBE Science Working Group and were provided by the NSSDC. The temperature fractional fluctuation (the magnitude of the CMBR anisotropy) can be related directly to the Newtonian gravitational potential via the Sachs–Wolfe formula.
- [16] Myron L. Good, Phys. Rev. **131**, 311 (1961).
- [17] R. B. Mann and U. Sarkar, Phys. Rev. Lett. **76**, 865 (1996)
- [18] J. N. Bahcall, *Neutrino Astrophysics*, Cambridge University Press (1988)
- [19] J. N. Bahcall and M. H. Pinsonneault, Rev. Mod. Phys. **67**, 781 (1995)
- [20] J. N. Bahcall *et al.*, Phys. Rev. **C54**, 411 (1996)

- [21] Hisakazu Minakata and Alexei Yu. Smirnov, Phys. Rev. **D54**, 3698 (1996)
- [22] D. V. Ahluwalia and C. Burgard, LA-UR-96-0862, gr-qc/9603008 (1996); *also* Ahluwalia and Burgard, LA-UR-96-2031, gr-qc/9606031 (1996).
- [23] J. R. Mureika, unpublished manuscript

Figure Captions

The following conventions are used for the figure conventions. The notation df_{21} , df_{31} on the plots corresponds to $2E\Delta f_{21}, 2E\Delta f_{31}$ which are expressed in units of 10^{18} MeV^{-1} . Also, $P = \langle P(\nu_e \rightarrow \nu_e) \rangle$, and $s_{2\theta_{12}}^2 = \sin^2 2\theta_{12}$, $s_{\theta_{13}}^2 = \sin^2 \theta_{13}$.

Figure 1: $\langle P(\nu_e \rightarrow \nu_e) \rangle$ curves for $s_{2\theta_{12}}^2 = 5 \times 10^{-3}$, $s_{\theta_{13}}^2 = 0.4$, $2E\Delta f_{31} = 2 \times 10^6$, $\Phi = \phi_{\odot}(r), \phi_{\odot}(R_{\odot})$.

Figure 2: $\langle P(\nu_e \rightarrow \nu_e) \rangle$ curves for $s_{2\theta_{12}}^2 = 0.8$, $s_{\theta_{13}}^2 = 0.4$, $2E\Delta f_{31} = 2 \times 10^6$, $\Phi = \phi_{\odot}(r), \phi_{\odot}(R_{\odot})$.

Figure 3: $\langle P(\nu_e \rightarrow \nu_e) \rangle$ curves for $s_{2\theta_{12}}^2 = 5 \times 10^{-3}$, $s_{\theta_{13}}^2 = 10^{-3}$, $2E\Delta f_{31} = 2 \times 10^6$, $\Phi = \phi_{\odot}(r), \phi_{\odot}(R_{\odot})$.

Figure 4: $\langle P(\nu_e \rightarrow \nu_e) \rangle$ curves for $s_{2\theta_{12}}^2 = 0.8$, $s_{\theta_{13}}^2 = 10^{-3}$, $2E\Delta f_{31} = 2 \times 10^6$, $\Phi = \phi_{\odot}(r), \phi_{\odot}(R_{\odot})$.

Figure 5: $\langle P(\nu_e \rightarrow \nu_e) \rangle$ curves for $s_{2\theta_{12}}^2 = 0.8$, $s_{\theta_{13}}^2 = 10^{-3}$, $2E\Delta f_{31} = 2 \times 10^6$, $\Phi = \phi_{\odot}(r), \phi_{\odot}(R_{\odot}), \phi_{SC}, \phi_{SD}$.

Figure 6: $\langle P(\nu_e \rightarrow \nu_e) \rangle$ curves for $s_{2\theta_{12}}^2 = 0.8$, $s_{\theta_{13}}^2 = 10^{-3}$, $2E\Delta f_{31} = 2 \times 10^6$, $\Phi = \phi_{\odot}(r), \phi_{\odot}(R_{\odot}), \phi_{SC}, \phi_{SD}$.

Figure 7: $\langle P(\nu_e \rightarrow \nu_e) \rangle$ surface for $s_{2\theta_{12}}^2 = 5 \times 10^{-3}$, $s_{\theta_{13}}^2 = 10^{-3}$, $\Phi = \phi_{\odot}(r)$.

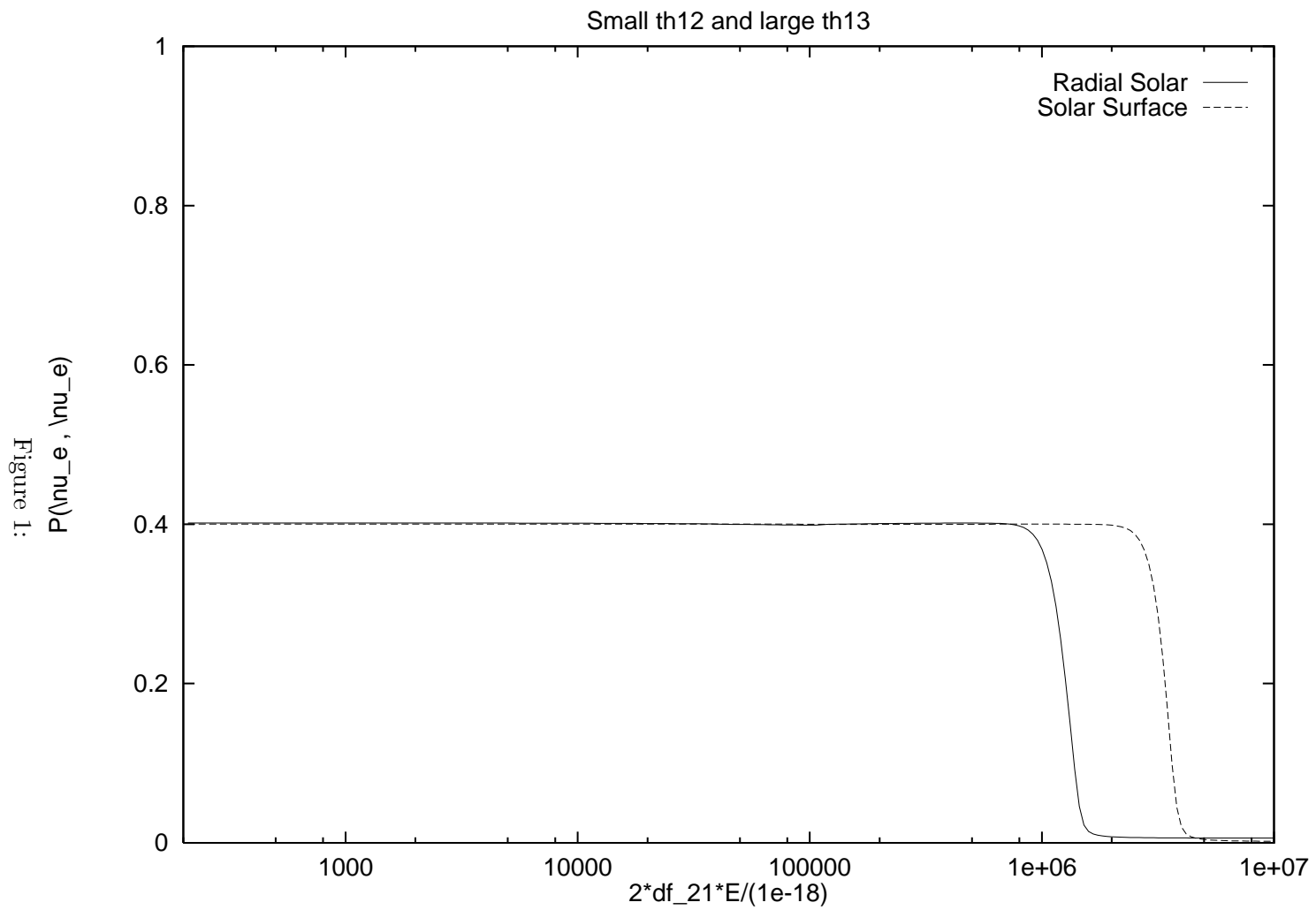
Figure 8: $\langle P(\nu_e \rightarrow \nu_e) \rangle$ surface for $s_{2\theta_{12}}^2 = 5 \times 10^{-3}$, $s_{\theta_{13}}^2 = 10^{-3}$, $\Phi = \phi_{SC}$.

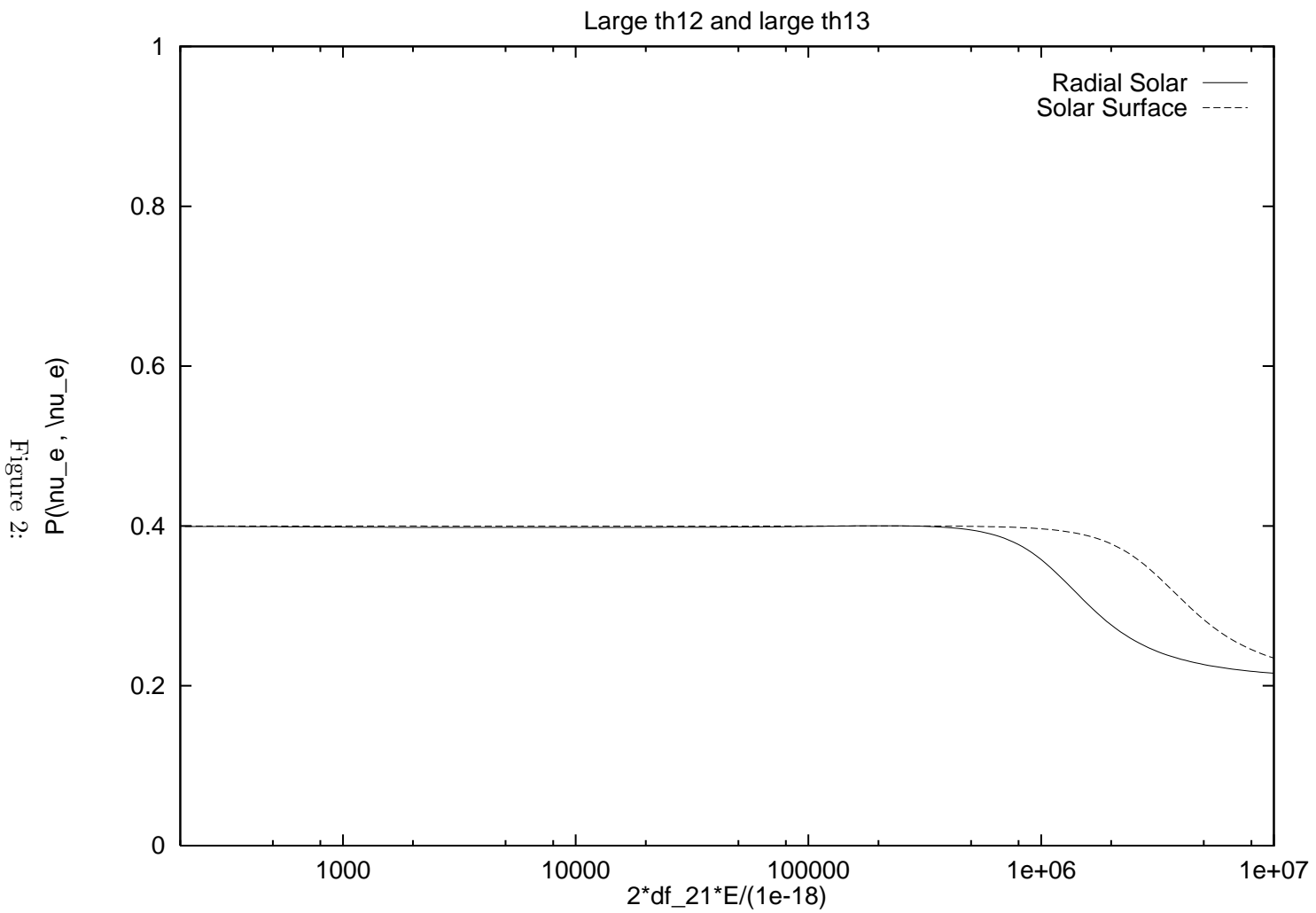
Figure 9: $\langle P(\nu_e \rightarrow \nu_e) \rangle$ surface for $s_{2\theta_{12}}^2 = 5 \times 10^{-3}$, $s_{\theta_{13}}^2 = 0.4$, $\Phi = \phi_{\odot}(r)$.

Figure 10: $\langle P(\nu_e \rightarrow \nu_e) \rangle$ surface for $s_{2\theta_{12}}^2 = 5 \times 10^{-3}$, $s_{\theta_{13}}^2 = 0.4$, $\Phi = \phi_{SC}$.

Figure 11: Overhead projection of Figure 9 showing resonance boundary and hierarchy breaking transition.

Figure 12: Overhead projection of Figure 10 showing resonance boundary and hierarchy breaking transition.





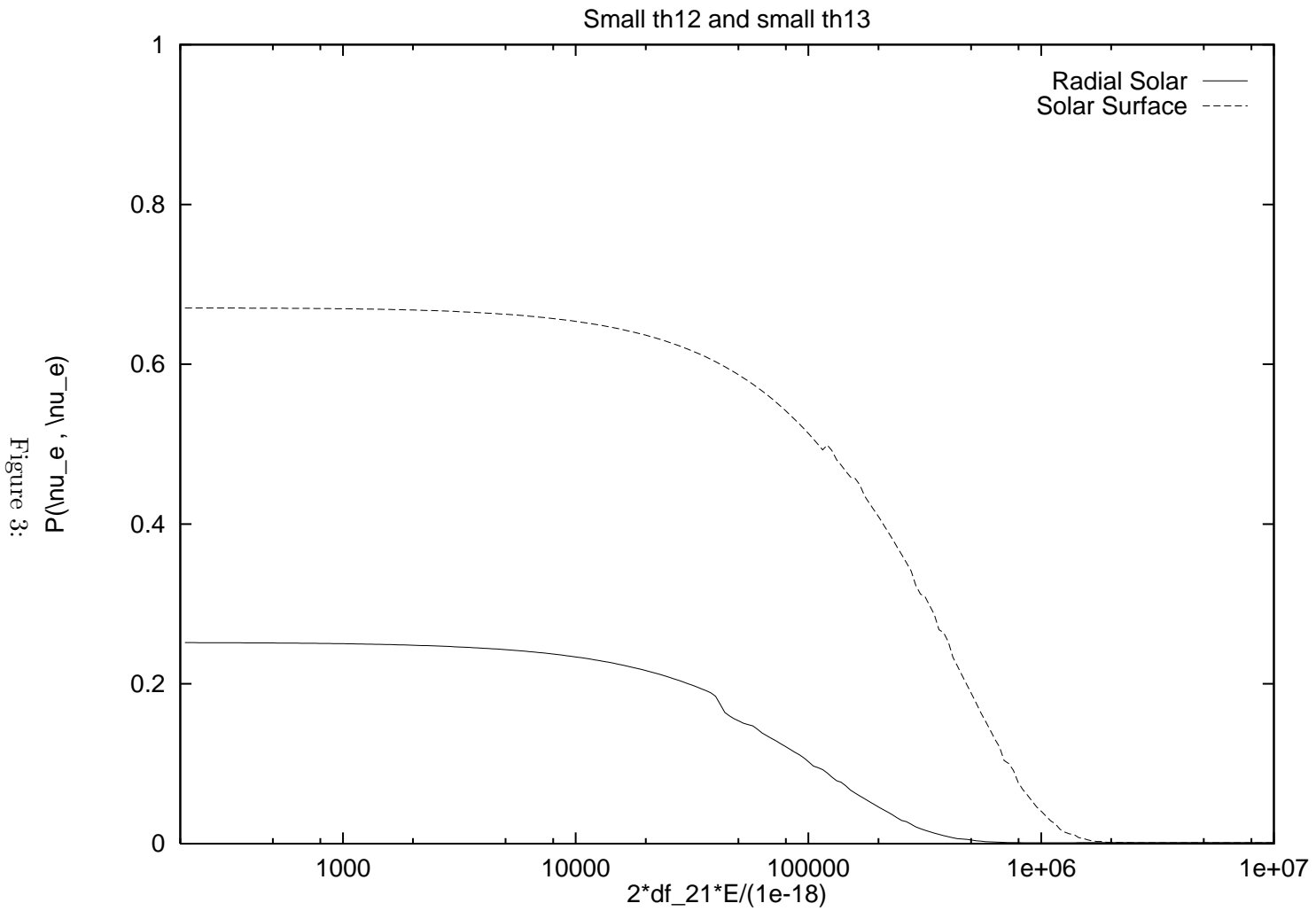


Figure 4:

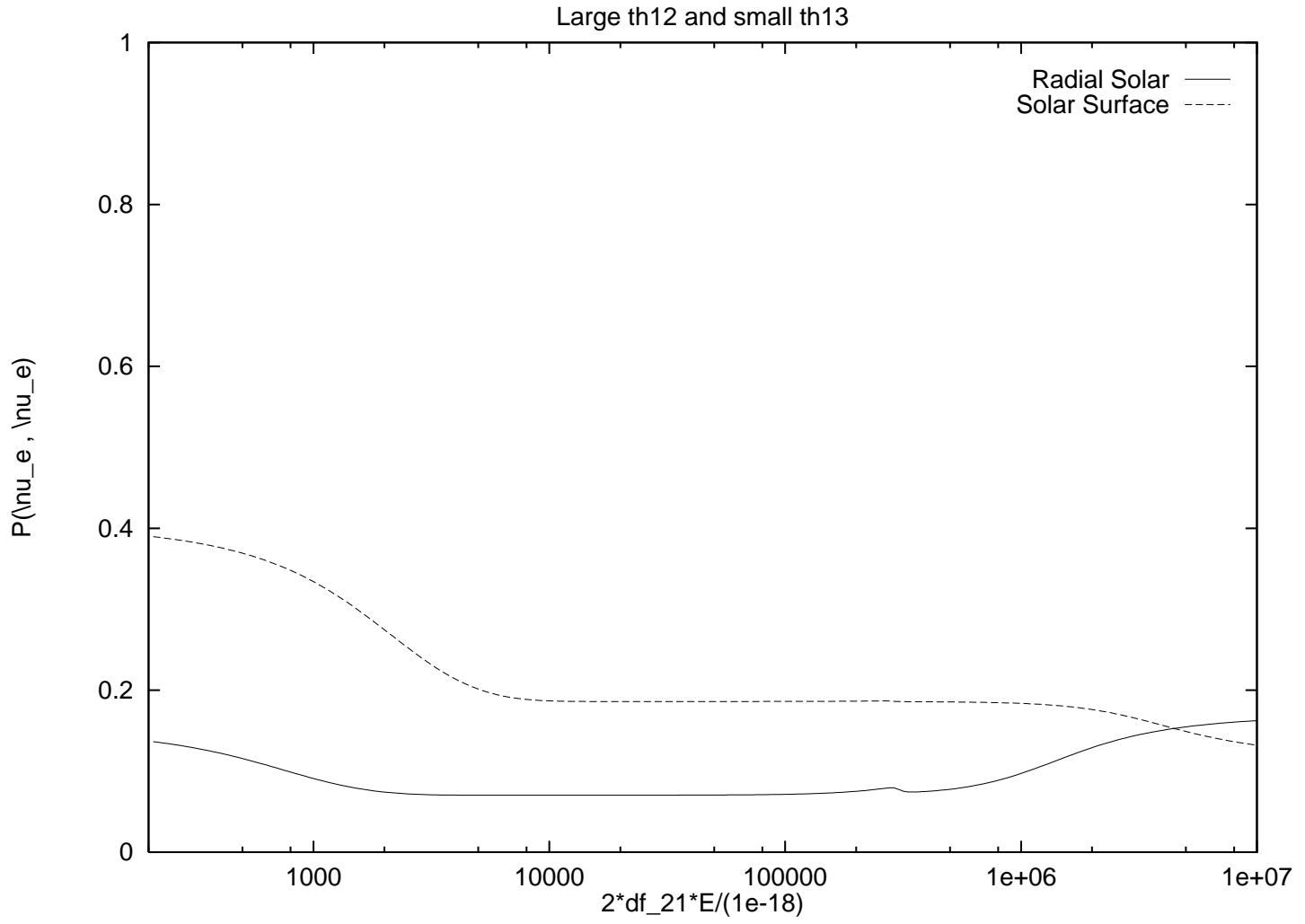
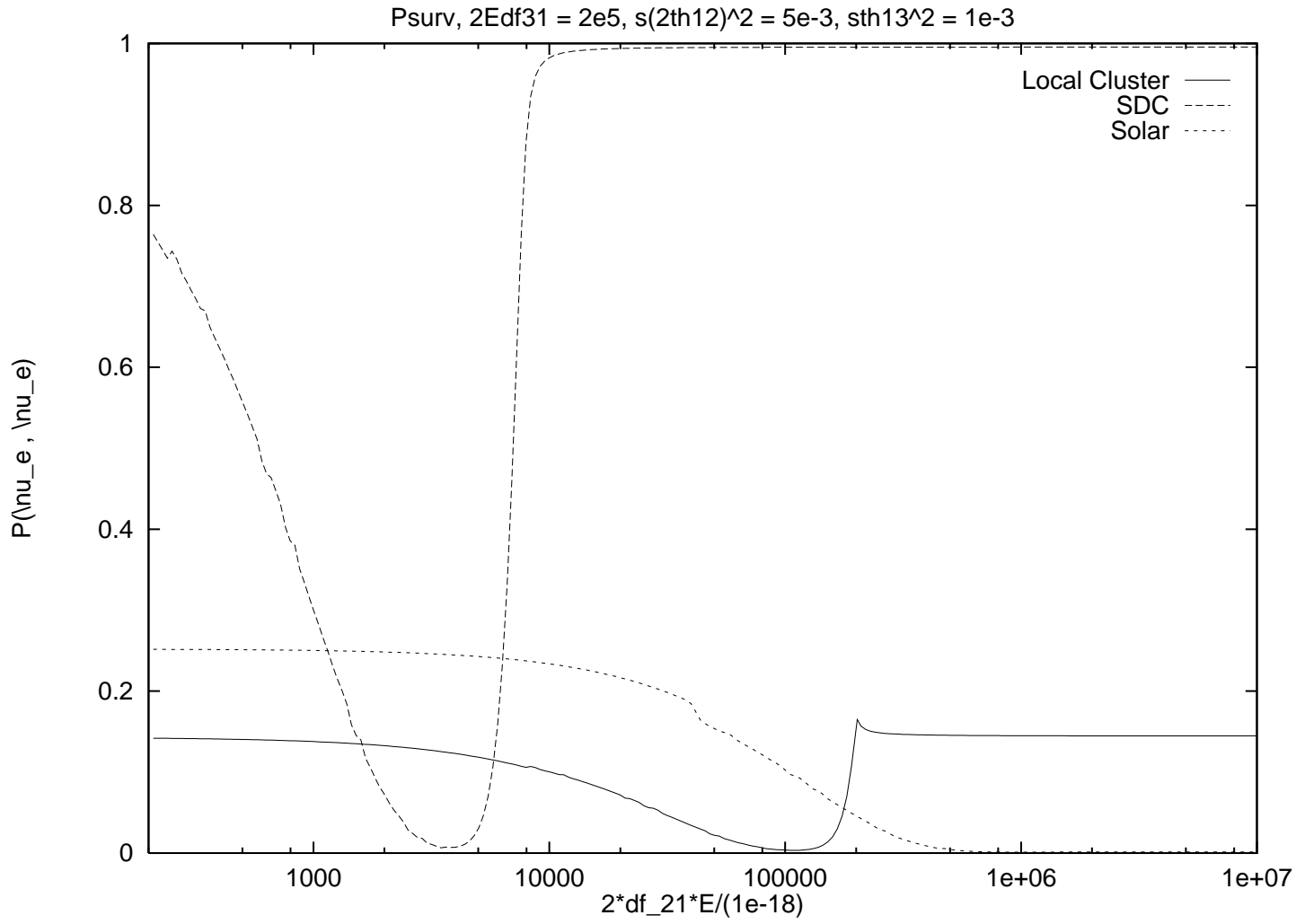
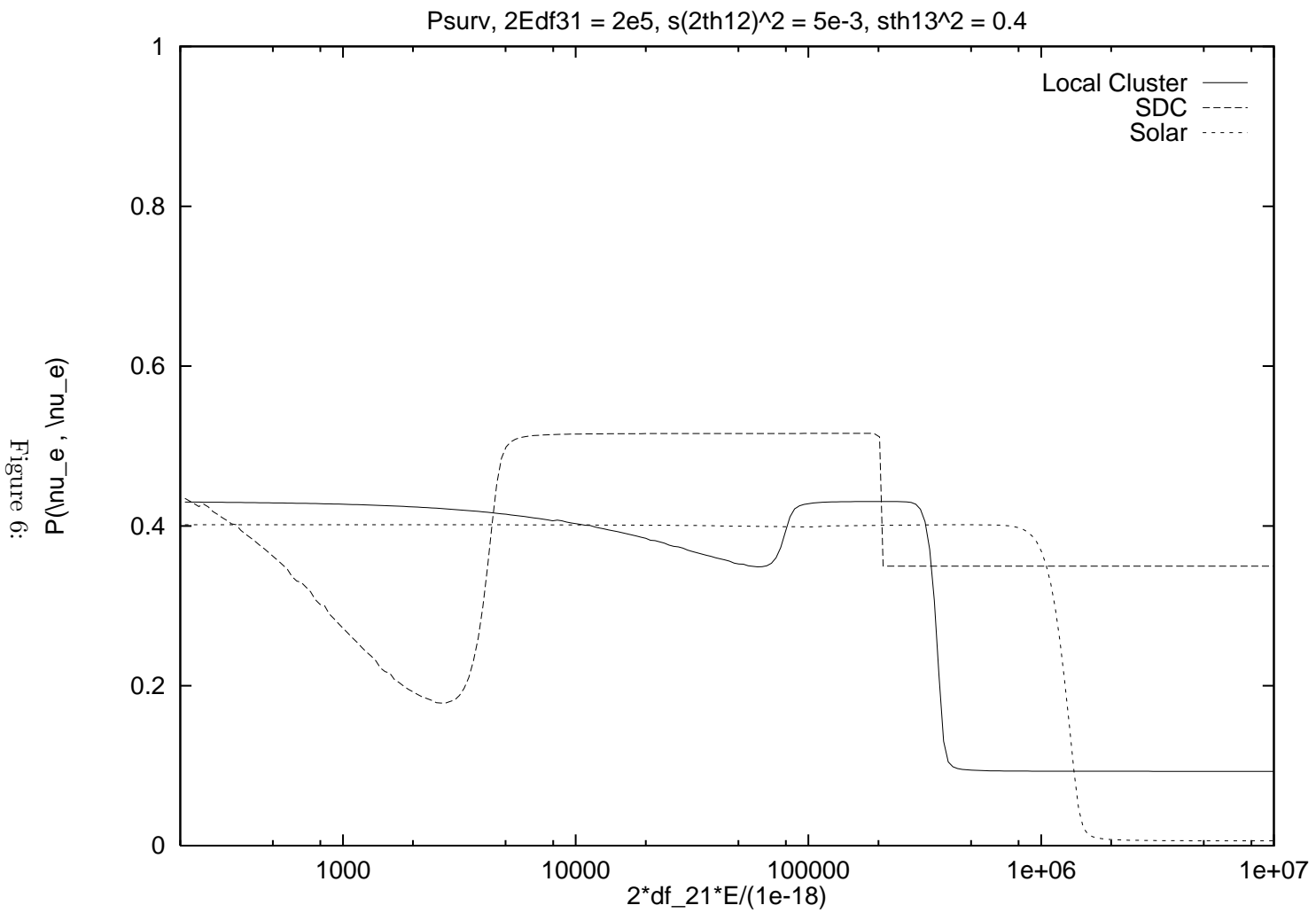


Figure 5:





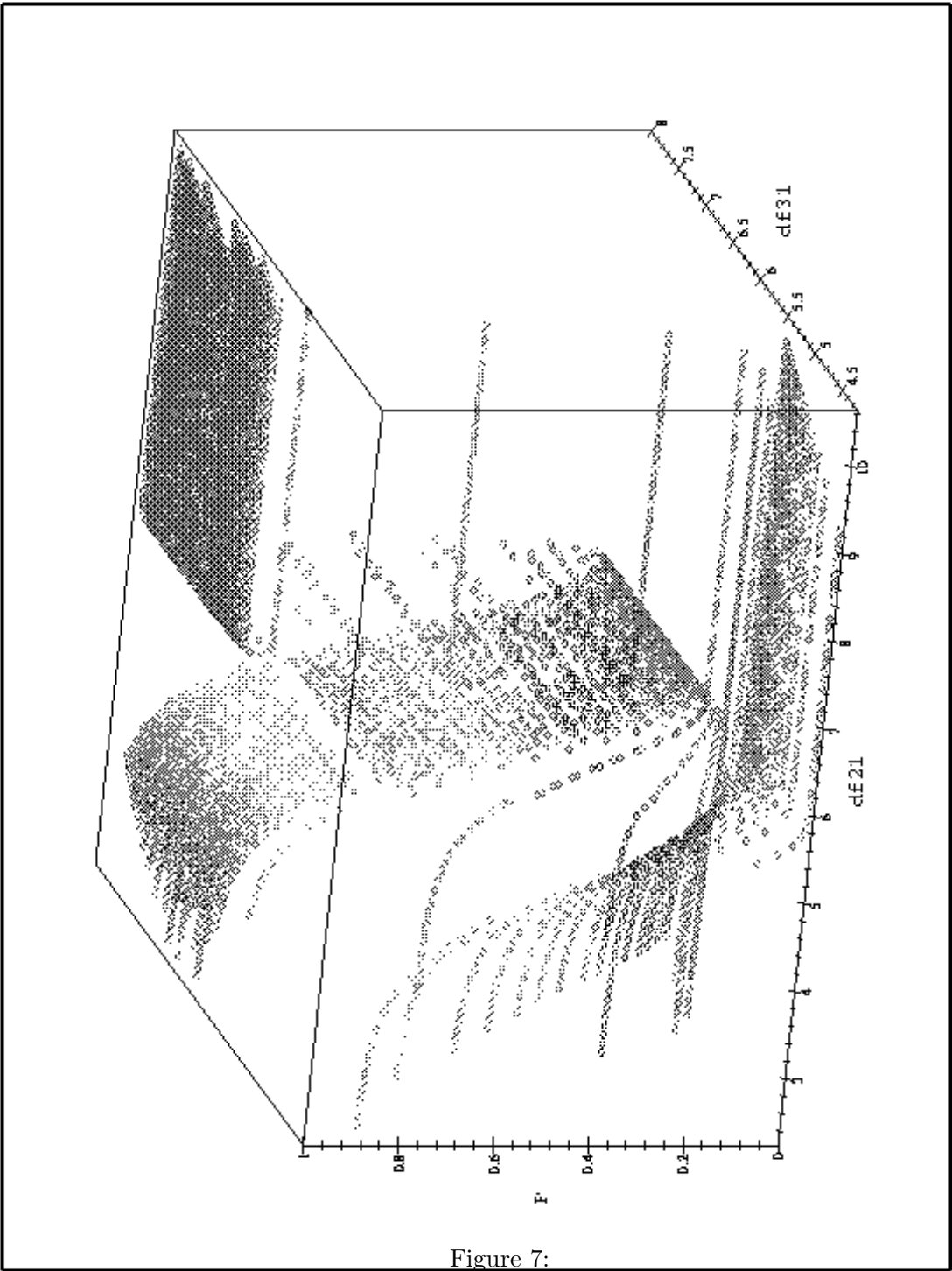


Figure 7:

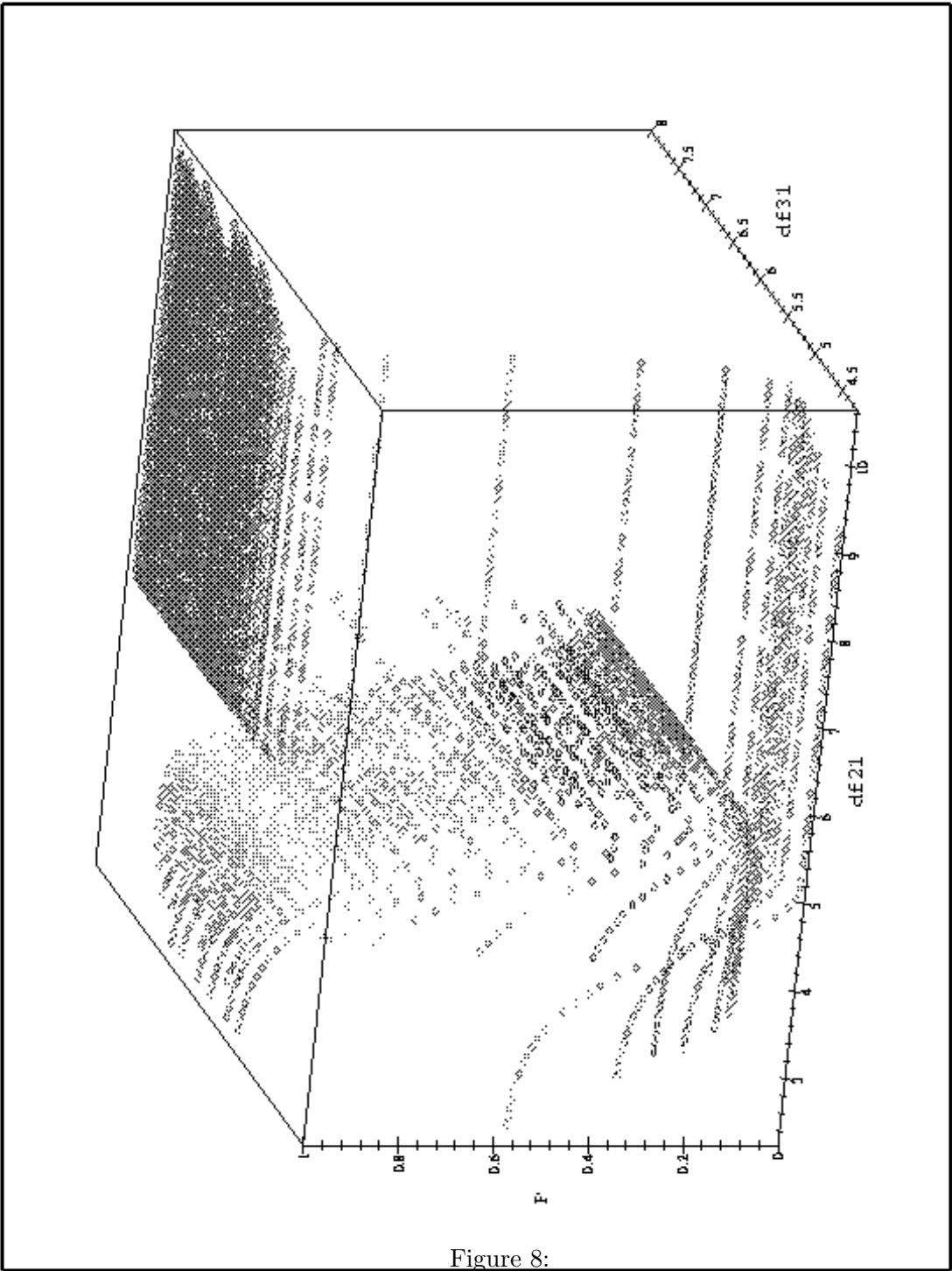


Figure 8:

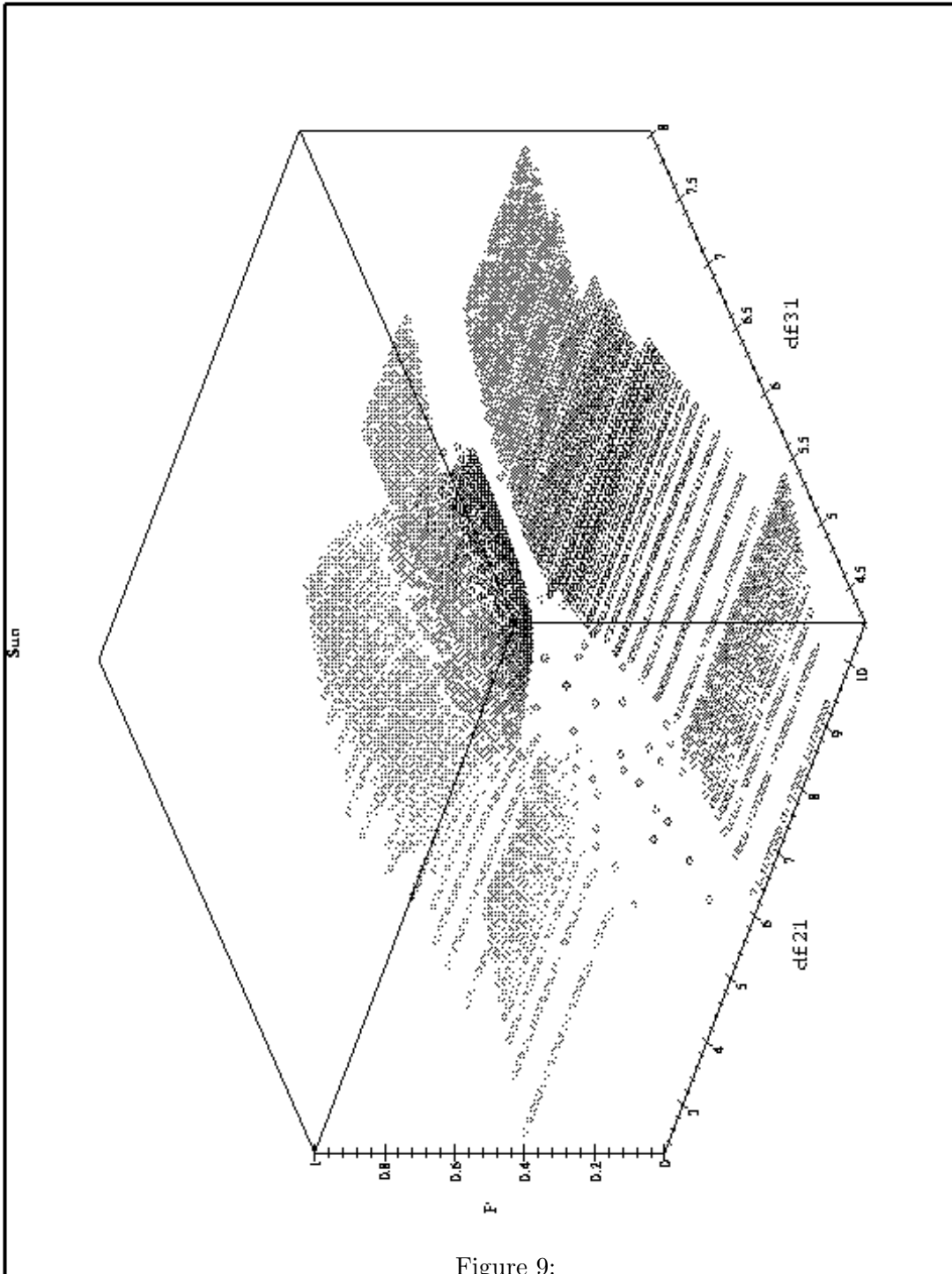


Figure 9:

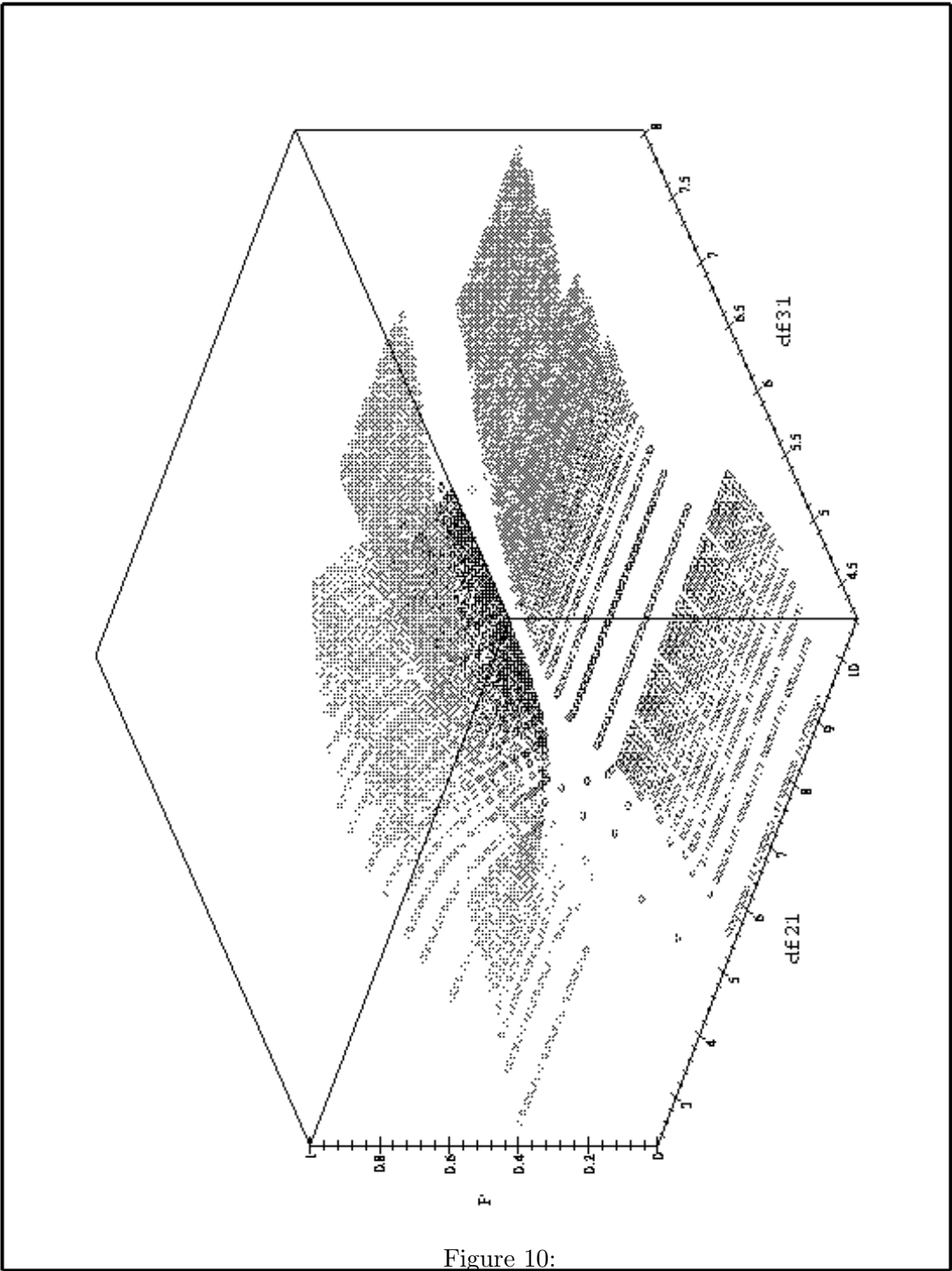


Figure 10:

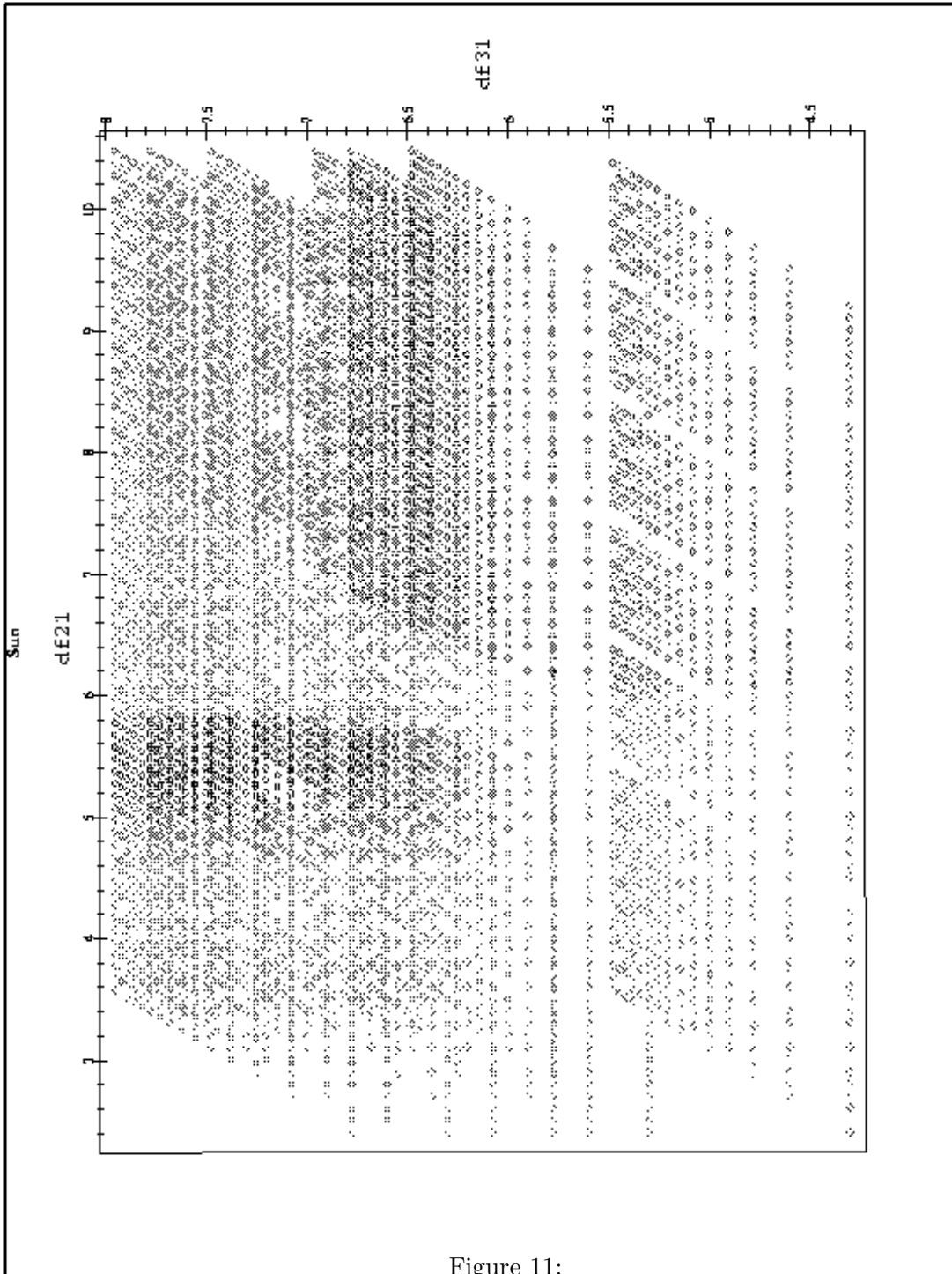


Figure 11:

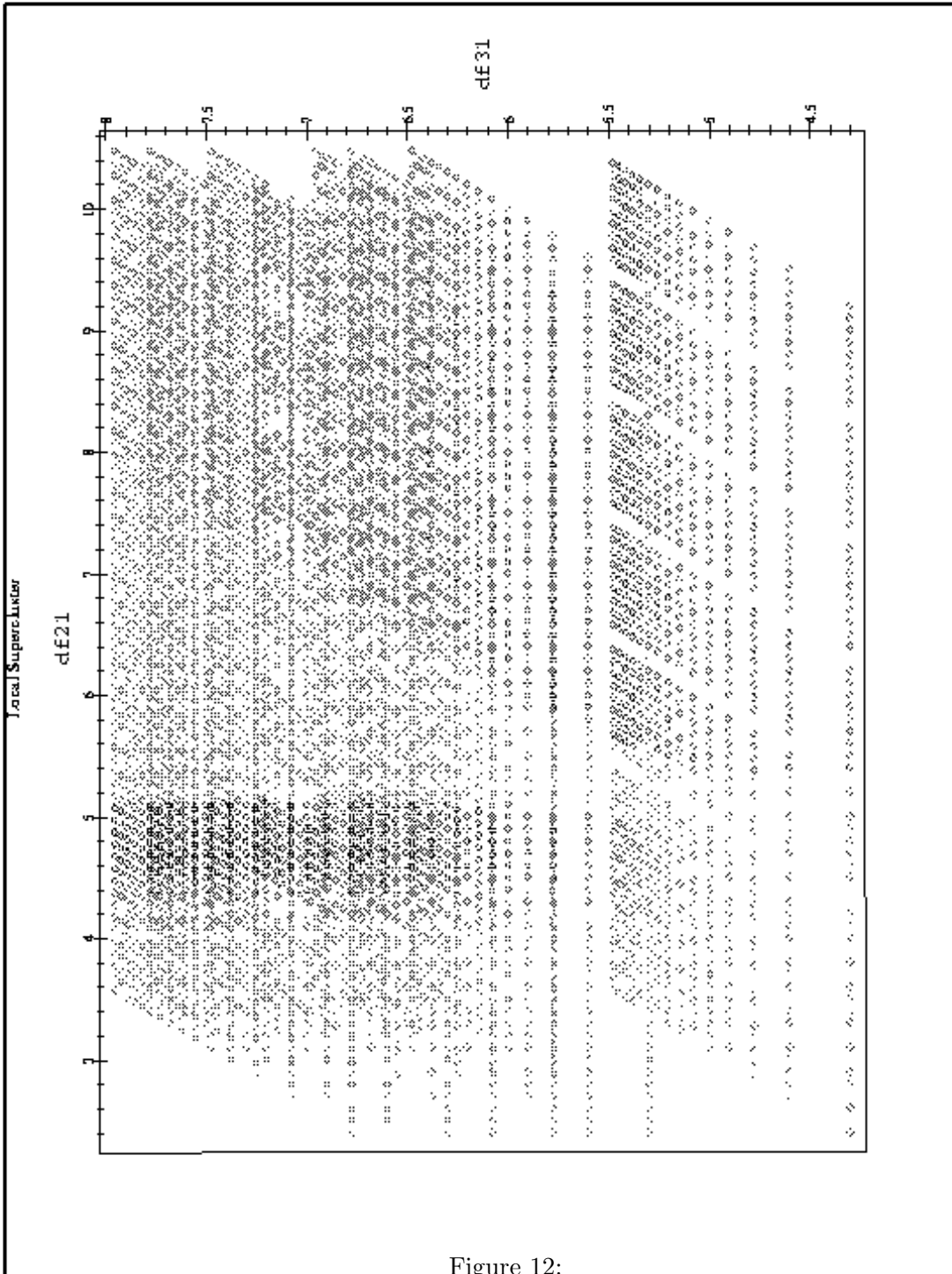


Figure 12: